Polyvinyl Chloride as a Multimodal Tissue-Mimicking Material with Tuned Mechanical and Medical Imaging Properties

Weisi Li[a)]
School of Mechanical Engineering, Dalian University of Technology, Dalian, Liaoning 110042, China
Mechanical Engineering Department, University of Michigan, Ann Arbor, MI 48109, USA

Barry Belmont, Joan M. Greve, Adam B. Manders, Brian C. Downey, Xi Zhang, and Zhen Xu
Biomedical Engineering Department, University of Michigan, Ann Arbor, MI 48109, USA

Dongming Guo
School of Mechanical Engineering, Dalian University of Technology, Dalian, Liaoning 110042, China

Albert Shih
Mechanical Engineering Department, University of Michigan, Ann Arbor, MI 48109, USA
Biomedical Engineering Department, University of Michigan, Ann Arbor, MI 48109, USA

Purpose: The mechanical and imaging properties of polyvinyl chloride (PVC) can be adjusted to meet the needs of researchers as a tissue-mimicking material. For instance, the hardness can be adjusted by changing the ratio of softener to PVC polymer, mineral oil can be added for lubrication in needle insertion, and glass beads can be added to scatter acoustic energy similar to biological tissue. Through this research, we sought to develop a regression model to design formulations of PVC with targeted mechanical and multimodal medical imaging properties.

Methods: The design of experiment was conducted by varying three factors – 1) the ratio of softener to PVC polymer, 2) the mass fraction of mineral oil, and 3) the mass fraction of glass beads – and measuring the mechanical properties (elastic modulus, hardness, viscoelastic relaxation time constant, and needle insertion friction force) and the medical imaging properties (speed of sound, acoustic attenuation coefficient, magnetic resonance imaging (MRI) time constants T_1 and T_2, and the transmittance of the visible light at wavelengths of 695 nm ($T_{\lambda 695}$) and 532 nm ($T_{\lambda 532}$)) on twelve soft PVC samples. A regression model was built to describe the relationship between the mechanical and medical imaging properties and the values of the three composition factors of PVC. The model was validated by testing the properties of a PVC sample with a formulation distinct from the twelve samples.

Results: The tested soft PVC had elastic moduli from 6 to 45 kPa, hardnesses from 5 to 50 Shore OOO-S, viscoelastic stress relaxation time constants from 114.1 – 191.9 s, friction forces of 18 gauge needle insertion from 0.005 to 0.086 N/mm, speeds of sound from 1393 to 1407 m/s, acoustic attenuation coefficients from 0.38 to 0.61 dB/cm/MHz, T_1 relaxation times from 426.3 to 450.2 ms, T_2 relaxation times from 21.5 to 28.4 ms, $T_{\lambda 695}$ from 46.8% to 92.6%, and $T_{\lambda 532}$ from 41.1% to 86.3%. Statistically significant factors of each property were identified. The regression model relating the mechanical and medical imaging properties and their corresponding significant factors had a good fit. The validation tests showed a small discrepancy between the model predicted values and experimental data (all less than 5% except the needle insertion friction force).

Conclusions: The regression model developed in this paper can be used to design soft PVC with targeted mechanical and medical imaging properties.

Keywords: tissue-mimicking materials, PVC, multi-modal, elastic modulus, ultrasound, needle

1. Introduction

Tissue-mimicking materials are widely used in clinical simulators and biomedical research. For clinical simulators, properties of the tissue-mimicking materials must be close to those of real tissue for surgeons, nurses, and caregivers to practice their clinical skills[1–4]. In medical research, tissue-mimicking materials play important roles as idealized tissue models to evaluate clinical devices, procedures, and systems, achieving more repeatable results in experiments than real tissues due to their stability, consistency, and uniform properties[5–7]. For instance, medical imaging researchers often utilize tissue-mimicking materials to calibrate equipment and develop new imaging methods[5]. A material that can be used for two or more imaging modalities is said to be multimodal. Such materials may also have mechanical properties to make clinical simulators behave analogously to real tissue while making imaging techniques more repeatable[8, 9]. The goal of this research was to study the mechanical and medical imaging properties of a multimodal tissue-mimicking material, namely polyvinyl chloride (PVC).

Common mechanical properties of tissue-mimicking materials include elasticity, viscoelasticity, and friction force during needle insertion. Elasticity, as quantified by an elastic modulus, is one of the most basic mechanical properties of tissue-mimicking materials, greatly affecting the haptics of simulators[10], force during needle insertion[11], and imaging quality in elastography[12]. It should be noted, however, that most tissue-mimicking soft materials are viscoelastic and this has a great effect on deformation[13–15]. The friction force further affects the haptic feel of a material during needle-based procedures[11, 16].

To be of the most use, tissue-mimicking materials should also target properties of soft tissues in one or more medical imaging modalities to make possible multi-faceted validation[17]. In ultrasound imaging technology development, tissue-mimicking materials are usually created with similar acoustic properties (i.e. speed of sound, acoustic attenuation, and acoustic impedance) to those of the soft tissues of interest[5-8]. Examples of ultrasound phantoms include agar based wall-less vessel phantoms for Doppler flow measurements[18], mixed agar and gelatin phantoms for elasticity imaging[19], and anthropomorphic phantoms made from multiple tissue-mimicking materials for medical training[20]. For MRI phantoms, tissue-mimicking materials must have physiologically relevant relaxation times, denoted T_1 and T_2 as the rate at which the longitudinal and the transverse magnetization vectors recover and decay, respectively[21]. The optical clarity of a tissue-mimicking material is also often desirable for medical imaging research as transparency can facilitate observation of internal

structures of a phantom, especially appealing for flow phantoms that might utilize particle image velocimetry (PIV), a non-intrusive technique to measure mean and instantaneous fluid velocities by recording the change in position of seeded particles[22].

Multimodal tissue-mimicking materials are valuable for medical imaging research because they can be used to develop and validate techniques across imaging modalities. Demonstrating the initial feasibility of such research, Hungr *et al*[16] made a multimodal prostate phantom using PVC for image guided biopsy procedures. The phantom had clearly distinguishable morphology visible via ultrasound, MRI, and computed tomography (CT). Chmarra *et al*[17] developed an agarose based liver phantom to get images from ultrasound imaging, MRI, and CT modalities similar to those of patients. Chen *et al*[9] created a polyvinyl alcohol (PVA) brain phantom that could be used to validate the results of ultrasound, MRI, and CT imaging.

Table I summarizes results of prior research on some mechanical and medical imaging properties of nine common tissue-mimicking materials (agar, agarose, gelatin, gellan gum, PVA, PVC, room-temperature vulcanizing (RTV) polymerized siloxanes (silicone), polydimethylsiloxane (PDMS), and polyurethane (PU)) and five types of tissues from human and animals (liver, brain, fat, muscle, and prostate). Agar, agarose, gelatin, and gellan gum are biopolymers, materials that contain a high mass fraction of water (>80%) making them similar in many respects to soft biological tissues[23]. However, due to the evaporation of water and bacterial growth, biopolymers are not stable for long-term storage and use[24]. PVA, RTV silicone, PDMS, PVC, and PU are common chemically synthesized polymers. Compared to biopolymers, these tissue-mimicking materials are more stable and durable[11, 25], though the lack of water in most chemically synthesized polymers makes them less similar to the real tissue, particularly in needle insertion procdures[16].

Of these materials, PVC has many advantages including high optical transparency and a hardness that is close to real tissue. Compared to biopolymers, PVC has the benefit of the ability to resist bacterial attack and moisture loss. As compared to the other listed chemically synthesized polymers, PVC is easier to manufacture than PVA, and has distinct acoustic advantages over silicone and PDMS for ultrasound imaging[26, 27]. The speed of sound of PVC, about 1400 m/s[16, 25, 28], is closer to that of generic human soft tissue, 1500 to 1600 m/s[29–32], than silicone (only about 1000 m/s)[26, 33] or PU (about 1800 m/s)[34, 35]. PVC also has a hardness and elastic modulus closer to soft tissues than PU and PDMS, which is an important factor to make the simulator have a tactile feeling similar to real tissue. In addition, the curing time of PVC is shorter than many RTV silicones. These advantages make PVC promising for clinical simulator production.

Properties of soft PVC – made by combining a PVC polymer solution and a softener – can be tailored to mimic different soft tissues by adjusting the ratio of the softener to polymer[16]. Similar to other chemically synthesized polymers, cured PVC does not have internal fluid components causing the friction force during needle insertion to feel unlike that of the same procedure in soft tissues[16]. To more closely align the properties of PVC with those of soft tissues in this regard, a lubricating

agent can be added into a PVC sample to simulate the interstitial fluids of tissue. Wang *et al*[11] utilized mineral oil as such a lubricating agent in RTV silicone tissue-mimicking materials and conducted needle insertion tests. With the addition of mineral oil, the hardness, elastic modulus, and needle insertion friction force of RTV silicone changed. The friction force decreased as the ratio of mineral oil in RTV silicone increased[11]. In this study, mineral oil was added to soft PVC primarily to act as a lubricant to decrease the needle insertion friction force. We also noted that during many needle based procedures, ultrasound imaging is used to monitor needle insertion path. PVC without any sort of additive looks very different from soft tissue under ultrasound examination because of its lack of specular reflectors. Glass beads were added to PVC to act as a scattering agent to enhance this scattering effect, making PVC appear more tissue-like under ultrasound examination. The change of the composition of PVC also affected other imaging properties such as optical clarity and the relaxation time constants of MRI. This paper presents the design and fabrication of soft PVC materials and evaluates their mechanical and medical imaging properties.

TABLE I. Properties of the tissue-mimicking materials and tissues

		Elastic Modulus E (kPa)	Needle Insertion Friction Force, f (N/mm) [Needle Diameter]	Speed of Sound c (m/s)	Acoustic Attenuation α (dB/cm/MHz)	T_1 (ms) [field strength] (Larmor Frequency)	T_2 (ms) [field strength] (Larmor Frequency)	Visible Light Transmittance
Biopolymers	Agar	52 – 499[36] 30 – 2300[37] 5 – 118[38]	–	1546 – 1554[39] 1564 – 1671[40]	0.32 – 0.53[39] 0.69 – 0.83[40]	1090 – 1150 [0.5-1.5 T][41] 380 – 2909 (100 MHz)[42]	42 – 50 [0.5-1.5 T][41] 24.7 – 143 (100 MHz)[42]	80% (380 – 1000nm)[43]
	Agarose	2 – 50[44] 1.5 – 1580[45]	–	1588.28 ± 15.72[46] 1500 – 1630[47]	1.28 ± 0.045[46]	1300 – 2600 [0.35 T][48] 1000 – 2743 [1.4 T][49]	20 – 130 [0.35 T][48] 23 – 278 [1.4 T][49]	40% (660nm, 50°C)[50]
	Gelatin	10 – 70[8] 36.7 – 111.5[51]	0.025 – 0.036 [1 mm][52]	1518 – 1535[8] 1535 – 1558[15]	0.35 – 0.5[8] 0.29 – 1.07[15]	369 – 498 (60 MHz)[8] 500 – 900 (10 MHz)[53]	28 – 63 (60 MHz)[8] 50 – 180 (10 MHz)[53]	98% (350 – 800 nm)[54]
	Gellan Gum	4.71 – 17.4[23] 0.15 – 148[55]	0.02 [1.27 mm][56] 0.0075 [1.27 mm][57]	1548 – 1584[23] 1579 – 1647[58]	0.64 – 0.88[23] 0.59 – 0.65[58]	–	–	–
Chemically Synthesized Polymers	PVA	25 – 615[14] 2.2 – 150[12]	–	1420 – 1464[12] 1520 – 1540[59] 1535 – 1559[60]	0.4 – 4(dB/cm)[12] 0.075 – 0.28[59] 0.5 – 1.2[60]	470 – 810 [1.5 T][61] 718 – 1034 [1.5 T][59]	40 – 90 [1.5 T][61] 108 – 175 [1.5 T][59]	95% (380 – 700 nm)[62] 40% (550nm)[63]
	PVC	3 – 200[16]	0.036 [0.46 mm][64]	1360 – 1400[16] 1400 – 1470[28] 1400 ± 20 [25]	0.14 – 1.16[28] 0.57 ± 1.01(dB/cm)[25]	–	–	–
	RTV Silicone	18 – 122[65] 9.5 – 96[13]	0.0175 – 0.1 [1.01 mm][11]	959 – 1113[33] 1069[26]	0 – 2.5[33] 1.43[26]	423 – 757 [3 T][66] 410 – 765 [1.4 T][67]	13 – 57 [3 T][66] 50 – 165 [1.4 T][67]	–
	PU	5 – 63.6 MPa[68] 10 – 100 MPa[69]	1 – 4 [3 mm][70]	1773 – 1994[35] 1750 – 1905[34]	1.22 – 1.54[71] 0.3 – 1.0[72]	306 ± 15 [1.5 T][71] 285 – 300 [1.5 T][73]	30 ± 1 [1.5 T][71] 38 – 41 [1.5 T][73]	90% (320 – 700 nm)[74] 92% (320 – 800nm)[75]
	PDMS	14.5 – 248.5[76]	–	1076 – 1119[27]	3.27 – 6.4[27]	716 [1.5 T][77]	68 [1.5 T][77]	85% (290 – 1100 nm)[78] 96% (400 – 700 nm)[79]
Tissue	Liver	0.94 (bovine, *ex vivo*)[80] 0.59 – 1.73 (human, *ex vivo*)[81]	0.025 [1.47 mm] (hog, *ex vivo*)[82] 0.012 [1.27 mm] (bovine, *ex vivo*)[83]	1584 – 1607 (human, *ex vivo*)[84] 1577 (bovine, *ex vivo*)[85]	0.8 – 1.5 (human, *ex vivo*)[84] 1 – 1.75 (bovine, *ex vivo*)[85]	443 [0.35 T] (human, *in vivo*)[86] 812 [3 T] (mouse, *ex vivo*)[87]	51 [0.35 T] (human, *in vivo*)[86] 42 [3 T] (mouse, *ex vivo*)[87]	–
	Brain	0.58 (human, *ex vivo*)[88]	0.00043 [0.235 mm] (rat, in vivo)[89]	1561 – 1565 (human, *in vivo*)[31]	0.58 – 0.8 (human, *ex vivo*)[32] 1.04 (human, *in vivo*)[31]	1300 [1.5 T] (human, *in vivo*)[90] 1820 [3 T] (Gray Matter) (mouse, *ex vivo*)[87]	75 [1.5 T] (human, *in vivo*)[90] 99 [3 T] (Gray Matter) (mouse, *ex vivo*)[87]	–
	Fat	2.5 (human, *in vivo*)[91]	–	1476 (human, *ex vivo*)[92] 1430 – 1480 (human, *ex vivo*)[93]	0.6 – 5.2 (human, *ex vivo*)[32]	266 [0.35 T] (human, *in vivo*)[86] 246 [0.35 T] (human, *in vivo*)[94]	57 [0.35 T] (human, *in vivo*)[86] 54.5 [0.35 T] (human, *in vivo*)[94]	–
	Muscle	1.5 (bovine, *ex vivo*)[80] 12.8 (human, *in vivo*)[95]	0.15 [1.6 mm] (pig, *ex vivo*)[96]	1555 – 1616 (bovine, *ex vivo*)[30]	1.03 (bovine, *ex vivo*)[30]	514 [0.35 T] (human, *in vivo*)[94]	32 [0.35 T] (human, *in vivo*)[94]	–
	Prostate	11 – 25 (human, *ex vivo*)[97] 1.3 – 5.6 (human, *ex vivo*)[98]	0.18 (insertion force) [1.27 mm] (human, *in vivo*)[99]	1614 (human, *ex vivo*)[29]	0.18 (human, *ex vivo*)[29]	1022 [1.5 T] (human, *in vivo*)[100]	86 [1.5 T] (human, *in vivo*)[100]	–

2. Materials and Methods

In this study, a general full factorial design of experiment (DOE) was created to study the effects of the ratio of softener to PVC polymer, mass fraction of mineral oil, and mass fraction of glass beads on mechanical and medical imaging properties of soft PVC. Factorial analysis was utilized to identify the statistical significance of three factors and a regression model was developed to find the quantitative relationship between PVC properties and three factors. A regression model was used to find values of three factors of the PVC as an example to achieve targeted mechanical and medical imaging properties and validate the results experimentally.

2.A. Design of Experiment

Three factors, the mass ratio of softener to PVC polymer solution ($R_{S/P}$), the mass fraction of the mineral oil (w_o), and the mass fraction of glass beads (w_g), were identified in the general full factorial DOE[101]. The $R_{S/P}$ greatly affected both the mechanical and medical imaging properties of PVC. Three levels of $R_{S/P}$ (0, 0.5, and 1) were examined for this experiment. PVC samples with $R_{S/P}$ in this range had similar hardness to that of soft tissue. The other two factors being relatively unknown (w_o and w_g) were tested at two levels. The highest w_o at which the mineral oil did not leak after curing was found to be 5%. This was the high value assigned to w_o. If the mass fraction of glass beads, w_g, was larger than 1%, the glass beads would precipitate during PVC curing. Two levels of the w_g were chosen to be 0 and 1%. In Table II, twelve combinations of factors and their levels of the DOE in this study are shown. The statistical analysis software Minitab® (Minitab Inc., State College, PA, USA) was used to do factorial analysis and build regression model.

TABLE II: Values of each factor at different levels for the DOE.

Factor	Level		
	Low	Middle	High
$R_{S/P}$	0	0.5	1
w_o	0	–	5%
w_g	0	–	1%

2.B. Soft PVC Fabrication

Soft PVC was made by mixing PVC polymer solution and a softener, in this case phthalate ester (both from M-F Manufacturing, Ft. Worth, TX, USA). In this study, mineral oil (W.S. Dodge Oil, Maywood, CA, USA) and spherical glass beads (50 μm average diameter) (Comco, Burbank, CA, USA) were added and mixed uniformly based on the DOE. Room temperature mixture (initially white and opaque) of the PVC polymer solution, the plastic softener, and additives (mineral oil and/or glass beads), was heated by a heat plate to 150°C with a magnetic bar stirring the liquid[25]. Increasing the temperature beyond 120 °C, the PVC monomers start to cross-link to polymers and the solution becomes transparent, reaching optimal cross-linking at 150 °C. After the mixture turned transparent, it was moved to a vacuum chamber to remove bubbles. Once vacuumed, the liquid mixture was poured into molds and cooled to room temperature. Three types of PVC samples, as shown Fig. 1, were made. The 50 mm long PVC samples (44.5 mm in diameter, Fig. 1(a)) were used for needle insertion experiments. The 20 mm long PVC samples (44.5 mm in diameter, Fig. 1(b)) were used for the indentation hardness, elastic modulus, acoustic properties and the MRI time constants. The samples with 10×10 mm^2 and a length of 40 mm (Fig. 1(c)) were made for visible light transmittance testing. The top surface of the sample was a concave meniscus, as seen in Fig. 1(a), due to the surface tension during cooling.

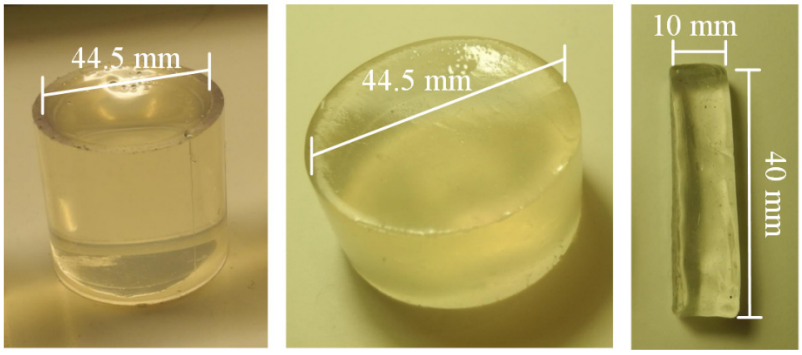

(a) (b) (c)

FIG. 1. Samples of soft PVC: (a) 44.5 mm in diameter and 50 mm in length, (b) 44.5 mm in diameter and 20 mm in length, and (c) 10×10 mm^2 and 40 mm in length.

2.C. Compression Test for Elastic Modulus Measurement

The method to measure the elastic modulus of PVC was through compression testing, a common method to obtain stress-strain relationships[16, 102]. Fig. 2 shows the PVC sample on an acrylic plate before compression by an aluminum plate mounted to the linear actuator (Model HLD60, Moog Animatics, Milpitas, CA, USA). The sample was compressed 9 mm (0.45 maximum engineering strain) at a speed of 0.5 mm/s. The force exerted on the sample was measured by a piezoelectric dynamometer (Model 9273, Kistler, Winterthur, Switzerland). The engineering stress vs. engineering strain curve indicated a nonlinear behavior of the material at large strains with a larger elastic modulus appearing at higher strains. The linear regime (below 0.15) was used to calculate the elastic modulus of the PVC sample using MATLAB® (Mathworks, Natick, MA, USA) with the least squares method. The average elastic modulus of three samples of each composition was used to represent the PVC material.

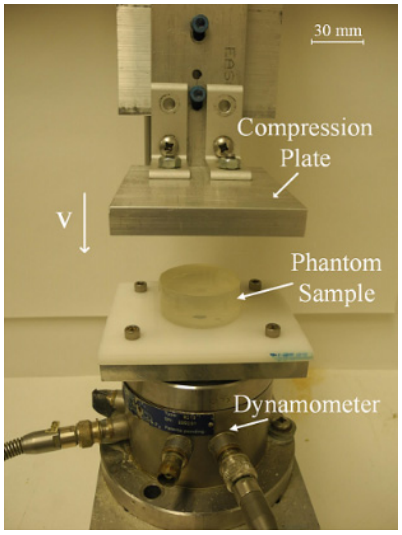

FIG. 2. Experimental setup of the elastic modulus measurement.

2.D. Shore Hardness Measurement

A Type OOO-S Shore durometer (Instron, Norwood, MA, USA) with a sphere surface indenter (10.67 mm in radius) was used to measure the hardness of the soft PVC, as shown in Fig. 3. Since the PVC is soft and the sample size is small, the deformation of the sample under the compression of the durometer was large and would be difficult to ensure full contact between the durometer plate and the sample in manual tests. To overcome this problem, the durometer was mounted to a computer-controlled linear actuator (Model HLD60, Moog Animatics, Milpitas, CA,

USA) to control its movement and position. After the indenter contacted the sample surface, the actuator drove the durometer down 5 mm until the durometer plate (see Fig. 3) touched the sample surface, and the reading on the dial, denoted as H, was taken as the Shore OOO-S hardness of this PVC sample. Three PVC samples (20 mm in length) were measured for each of the 12 groups of PVC.

The indentation test results were used to calculate the elastic modulus of the sample as the indentation force can be obtained based on the American Society for Testing and Materials (ASTM) Standard D2240-05[103],

$$F = 0.01756H + 0.167 \tag{1}$$

where H is the durometer reading and F is the indentation force. The indentation depth h of the indenter can be calculated with H[103].

$$h = 0.005(1 - \frac{H}{100}) \tag{2}$$

Based on the model of Briscoe *et al*[104], the elastic modulus E of the PVC sample can be calculated with the indentation force, F, indentation depth, h, Poisson's ratio, ν, and the radius of the indenter spherical surface, R.

$$E = \frac{3(1-\nu^2)F}{4\sqrt{R}h^{3/2}} \tag{3}$$

The Poisson's ratio of soft PVC was assumed to be 0.49 via the results of Naylor[105]. The R of the indenter is 10.7 mm. The elastic modulus calculated from the hardness was compared to that measured by the compression test with the difference ratio $(E_{test} - E_{cal})/E_{test}$.

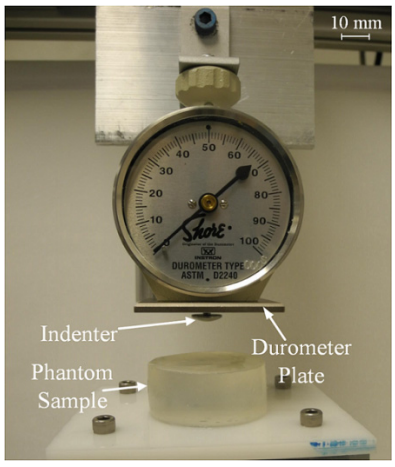

FIG. 3. Experimental setup for measuring hardness of the soft PVC.

2.E. Viscoelastic Relaxation Time Constant Measurement

Soft PVC is a viscoelastic material[16]. If a constant strain was applied to a sample, the stress would relax over time[106]. To characterize PVC's viscoelastic properties, the experimental setup used for the compression test of the previous section was modified such that the sample was compressed with a strain of 0.15 at a rate of 1.67 mm/s and then this strain was kept constant for 300 s. The force on the sample during this time was measured by the dynamometer used in elastic modulus testing and the obtained stress-time curves were used to estimate the stress relaxation time constants of the material. The MATLAB® curve fitting toolbox was used to fit the stress relaxation curves with the nonlinear least square method.

2.F. Needle Insertion Friction Force Measurement

Needle insertion experiments were used to assess the friction forces between the PVC and a needle. The experimental setup for needle insertion (Fig. 4) was designed to insert an 18 gauge (1.01 mm diameter) stainless steel solid trocar with 10° bevel angle three-plane diamond tip into the PVC. For a solid needle insertion procedure, when the needle tip was inside the sample, the axial force was the sum of cutting force at the tip and the friction force on the surface of the needle rod. After the needle tip punched out of the sample, only the friction force remained on the needle. Similar to the method used by Wang *et al*[11], after the needle reached the farthest position in each insertion, it was retracted and advanced three times to test the friction force exclusively in cyclic insertion.

To facilitate this measurement, a needle was fixed to a custom designed needle holder that was mounted to a stack of linear stages in parallel. Two linear stages (Model 200cri, Siskiyou Instrument, Grants Pass, OR, USA) were used to drive the needle into the PVC sample with the same speed in the same direction – the combination of the two stages in parallel allowed the distance over which the needle was moved to be longer (insertion speed of 0.7 mm/s and an insertion distance of 70 mm). Another linear stage (Model 100cri, Siskiyou Instrument, Grants Pass, OR, USA) was used to adjust the position of the needle. A piezoelectric dynamometer (Model 9256, Kistler, Winterthur, Switzerland) was used to measure the force during the needle insertion. A cylindrical PVC sample (44.5 mm in diameter and 50 mm in length) was secured by a holder to top of the dynamometer. For each sample,

the insertion procedure was repeated 6 times along a concentric circle of the cylinder by rotating the sample 60° between each run.

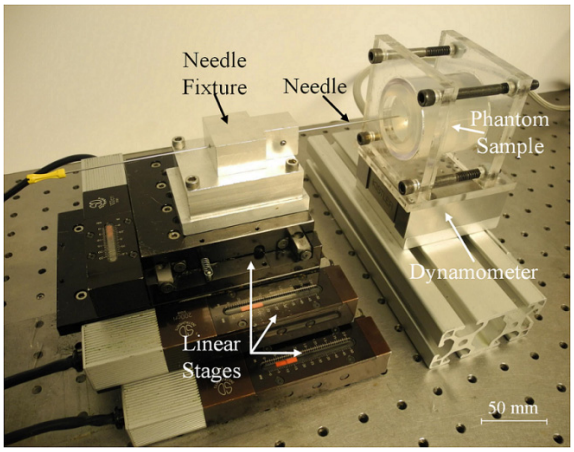

FIG. 4. Experimental setup of the needle insertion tests.

2.G. Acoustic Properties Measurements

The speed of sound and acoustic attenuation coefficient of the PVC samples were measured using the method described by Xu and Kaufman[107]. A PVC sample was placed in a degassed water tank between an unfocused ultrasound transducer (3.5 MHz, 13 mm aperture, Aerotech Laboratories, Lewistown, PA, USA) and a hydrophone (HNR-0500, ONDA Corporation, Sunnyvale, CA, USA). To ensure the acoustic path length through the sample was equal to the thickness of the sample, the hydrophone was aligned at a point perpendicular to the center of the transducer surface and the plane of the sample was oriented parallel to the transducer surface (see Fig. 5). The thickness of each sample was measured with a caliper. The unfocused transducer generated and sent acoustic pulses through the samples that were then received by the hydrophone. The received acoustic signal was captured and displayed using an oscilloscope (1 GHz, LC574AL, LeCroy, Chestnut Ridge, NY, USA). To measure the acoustic properties, acoustic pulses were first generated and measured without a sample between the transducer and the hydrophone, giving a baseline reading of the time delay and amplitude of the acoustic signal in water. Once a baseline was established, a sample was placed between the transducer and the receiver. With the sample in between, the delay of the received signal was altered and the amplitude was reduced. Knowing the delay of the received signals with and without the sample in the path, the speed of sound in the PVC material could be calculated by

$$c = \frac{\delta}{t_1 - \frac{t_0 c_w - \delta}{c_w}} \tag{4}$$

where c is the speed of sound in the sample, δ is the thickness of the sample, c_w is the speed of sound in water, t_0 is the time delay without the sample, and t_1 is the time delay with the sample. Taking the ratio of the signal amplitude with and without the sample in the path allowed us to calculate the attenuation coefficient with

$$\alpha = -20 \log \frac{A_1}{A_0} / \delta / f \tag{5}$$

where α is the acoustic attenuation coefficient, A_1 is the received signal amplitude with the sample in the path, A_0 is the signal amplitude without the sample, δ is the thickness of the sample in centimeter, and f is the frequency of the ultrasound wave (3.5 MHz for this study). To test the scattering effect of the glass beads, ultrasound images of the PVC samples with and without glass beads were recorded with a hand held ultrasound probe (Vascular Access 99-5930, Interson Medical Instruments, Pleasanton, CA, USA) connected to a computer via universal serial bus (USB).

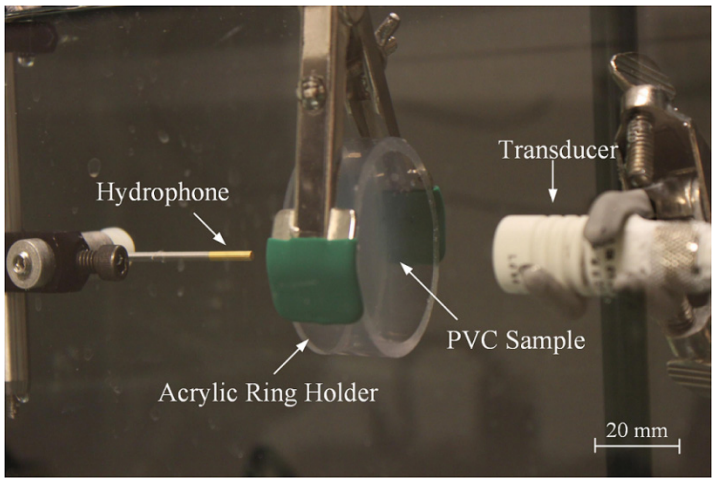

FIG. 5. Picture of the experimental setup for acoustic properties measurement.

2.H. Optical Clarity Characterization

In optics and spectroscopy, transmittance is the fraction of incident light (electromagnetic radiation) at a specified wavelength that passes through a sample[108]. In this study, transmittance was chosen to represent the

transparency of the PVC material. The samples were placed into 4.5 mL poly(methyl methacrylate) (PMMA) cuvettes (dispolab Kartell) with de-ionized water. Samples were chosen with minimal surface variations to lessen the effects of surface properties on the measurements. A spectrophotometer (Biomate 3S, Thermo Scientific, Waltham, MA, USA) was used to measure the transmittance of visible light (380 nm to 750 nm in 1 nm increments) through each of the twelve types of samples. A qualitative assessment of the optical clarity of PVC was also made by placing a sample over a checkerboard pattern and observing its clarity.

2.I. MRI Time Constant T_1 and T_2 Measurements

The order of the samples was chosen randomly for imaging and personnel acquiring and analyzing the MRI data were blinded to the contents of the samples. All MRI was performed at 7.0 T using a Direct Drive Console (Agilent Technologies, Santa Clara, CA, USA) and a 72 mm inner-diameter transmit-receive radiofrequency (RF) volume coil (Rapid Biomedical, Rimpar, Germany). Prior to imaging, the samples were fitted into a plastic ring to fix the sample and wrapped in parafilm in order to avoid contamination of the equipment. The wrapped samples were taped onto a plastic tray within the RF coil to further minimize motion. Following scout imaging to confirm proper placement of samples, a spin-echo sequence was used to acquire data using a 64 × 64 matrix, zero-filled to 128 × 128. For calculations of T_1, the spin-echo sequence included a preparatory inversion pulse (180°) and the inversion time (*TI*) was arrayed with values relevant to approximate T_1 values for these samples (field of view = 60 × 60 mm^2, slice thickness = 2 mm, 1 slice, repetition time = 2550 ms, echo time (*TE*) = 15 ms, inversion time *TI* = 50, 400, 1100, and 2500 ms, number of excitations (*NEX*) = 1, acquisition time ~ 11 min). For calculations of T_2, the spin-echo sequence included an array of *TE* values relevant to T_2 fitting for these samples (field of view = 60 × 60 mm^2, slice thickness = 2 mm, 1 slice, repetition time = 2550 ms, *TE* = 11, 28.25, 45.5, 62.75, and 80 ms, *NEX* = 1, acquisition time ~ 13 min). Prior to data acquisition on all samples, a subset was used to determine the appropriate *TI*'s and *TE*'s. Although the Larmor frequency of the samples differs from water based substances, using the automatic prescan settings in preparation for acquiring images, the MRI system automatically detected and assigned the appropriate frequency to use for imaging these samples. Due to the dependence of T_1 on temperature[109], ambient temperature near to the sample was measured using a fiber optic temperature probe (SA Instruments, Stony Brook, NY, USA).

Images were analyzed using MRVision (Winchester, MA, USA) to produce a T_1 and T_2 map for each sample. Respective image sets were fitted to the equation for T_1 mapping,

$$SI = M_0[1-(1+a)e^{TI/T_1}] \tag{6}$$

and for T_2 mapping,

$$SI = M_0 e^{-TE/T_2} \tag{7}$$

where SI is the signal intensity of a given image, M_0 is the final or initial signal intensity (for T_1 and T_2 mapping, respectively), and a is the adjusting coefficient for potential incomplete T_1 relaxation due to repetition time used. The T_1 mapping method provided through MRVision uses a nonlinear least squares fit to the set of inversion recovery weighted images, with fitting parameters of M_0, T_1, and a and input parameters being the TI values. Initial guesses for the fitting parameters are automatically estimated for each pixel using the final signal level for M_0, an estimation of T_1 from the approximate null point, and a = 1 (which would make the argument (1 + a) = 2, or complete T_1 relaxation). The T_2 mapping method provided through MRVision uses a linear regression analysis on the set of T_2 weighted images, with fitting parameters M_0 and T_2 for each pixel and input parameters being the TE values. From the resultant maps, the mean values and standard deviations of T_1, a, and T_2 were measured using a region of interest located approximately at the center of the sample, trying to avoid potential artifacts at the interface between the sample and plastic ring or air bubbles within the sample.

3. Results and Discussion

3.A. Elastic Modulus

A representative engineering stress vs. engineering strain curve of a PVC sample is shown in Fig. 6. In the beginning, the stress increased with the strain linearly and after the strain exceeded approximately 0.15, the stress began to increase with stain nonlinearly. To get the elastic modulus, E, in the linear elastic region of the material, the measured stress data with strain below 0.15 was used. Fig. 7 shows the elastic modulus of 12 PVC samples measured through compression test. The error bars (in black color) represent the standard deviation of the value of the three samples for each PVC material. All values were seen to be below 50 kPa. E decreased with increasing

$R_{S/P}$. The elastic moduli of PVC with $R_{S/P}$ values of 0 were about 5 times larger than those with an $R_{S/P}$ of 1 (all below 10 kPa). The PVC samples with mineral oil had a smaller E than those without mineral oil. The glass beads tended to slightly lower E of the PVC. Consulting the list of tissue properties seen in Table I, our PVC samples were found to be within the range of *in vivo* human muscle and *ex vivo* human prostate.

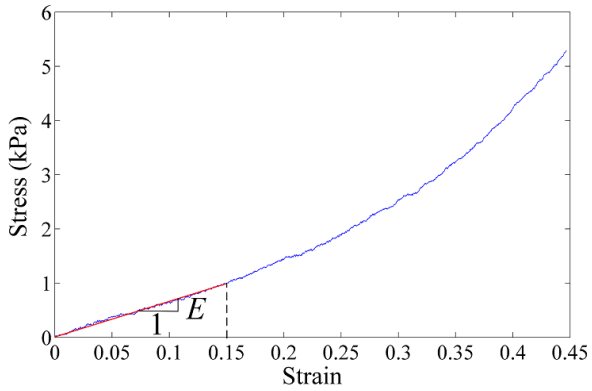

FIG. 6. The stress-strain curve of the PVC material with $R_{S/P}$ of 1, w_o of 0, and w_g of 0.

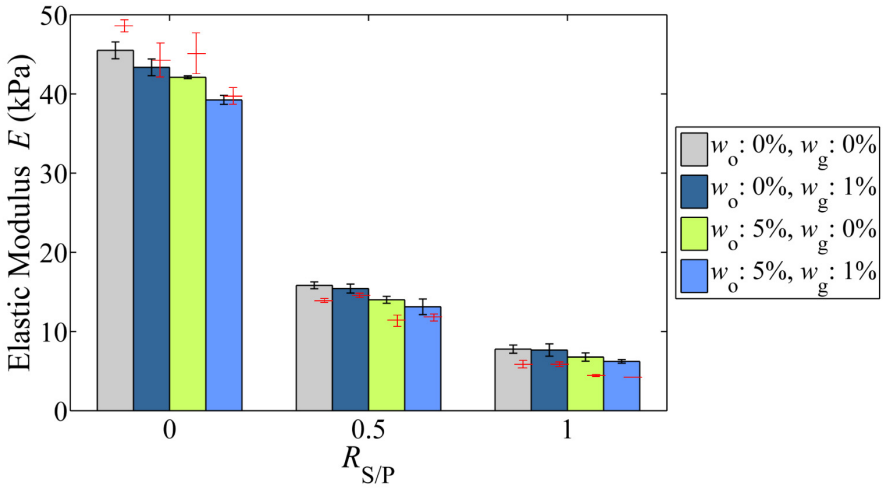

FIG. 7. The elastic modulus of 12 PVC samples obtained from the compression test (red line representing the elastic modulus estimated based on the Shore hardness).

3.B. Shore Hardness

The Shore OOO-S hardness, H, of the PVC with different compositions is shown in Fig. 8. The error bars represent the standard deviation of the value of three samples for each PVC material. These PVC samples were very

soft with H typically below 50. PVC samples with $R_{S/P}$ values of 0 were observed to have a hardness 5 times greater than those with $R_{S/P}$ values of 1. The addition of mineral oil also lowered H by 10% to 40%.

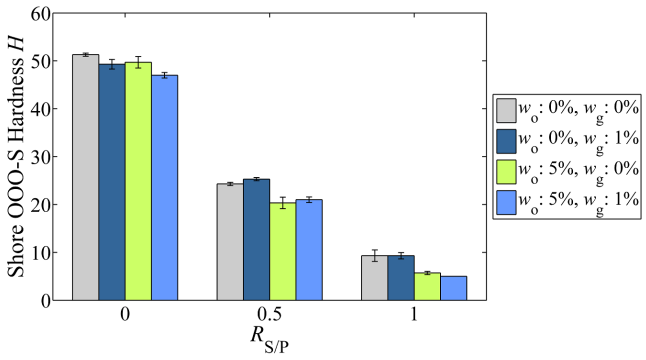

FIG. 8. The hardness of 12 PVC samples measured by durometer.

The elastic modulus can also be estimated based on the Shore hardness (Equations (1) to (3)). Red lines in Fig. 7 represent the elastic moduli calculated based on the durometer Shore hardness indentation test. For harder PVC samples ($R_{S/P}$ = 0), the E estimated based on H was about 7% greater than that measured via the compression test. This trend was reversed when the PVC material was softer ($R_{S/P}$ = 0.5 and 1). In general, the durometer indentation test, which is easier to perform than the compression test, can be utilized to predict the E for the PVC samples with less than 30% error.

3.C. Viscoelastic Relaxation Time Constant

The viscoelastic stress relaxation time constant of the PVC sample was investigated by fitting the experimentally measured stress-time curve with a five-parameter generalized Maxwell model to obtain the viscoelastic relaxation time constants[110]. The equation to describe the stress relaxation behavior in five-parameter generalized Maxwell model is:

$$\sigma = \sigma_0 + \sigma_1 e^{-t/\tau_1} + \sigma_2 e^{-t/\tau_2} \tag{8}$$

where σ_0 is the stable stress, σ_1 and σ_2 are stress constants, and τ_1 and τ_2 are relaxation time constants for two Maxwell branches. In the data fitting, the σ_0 was appointed with the value of the stress at 300 s to avoid the fitted

stable σ deviating too far from the measured value. This generalized Maxwell model can fit the stress relaxation curve accurately ($R^2 = 0.99$), as shown in Fig. 9.

Among five parameters of this model, the relaxation time constants τ_1 and τ_2 are parameters of the viscous property. To establish a regression model of the relaxation time constant, the larger of τ_1 and τ_2 was chosen to represent the principle relaxation time constant τ of the stress relaxation behavior. The τ, as shown in Fig. 10, is increased with $R_{S/P}$. With the same $R_{S/P}$, the addition of mineral oil decreased the τ. The error bars represent the standard deviation of the value of the three samples for each PVC material.

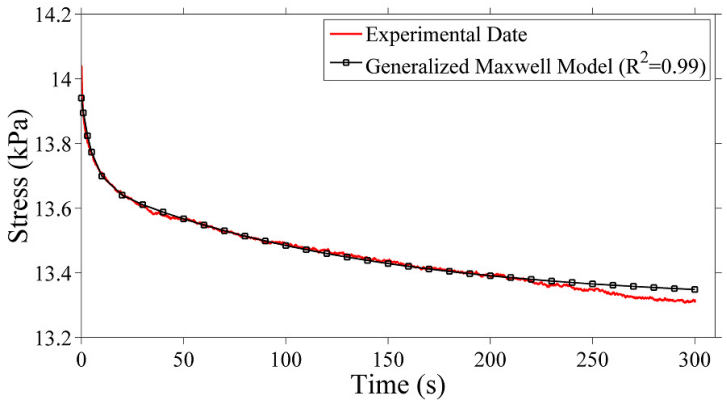

FIG. 9. The sample data of viscoelasticity measurement fitted with five-parameter generalized Maxwell model.

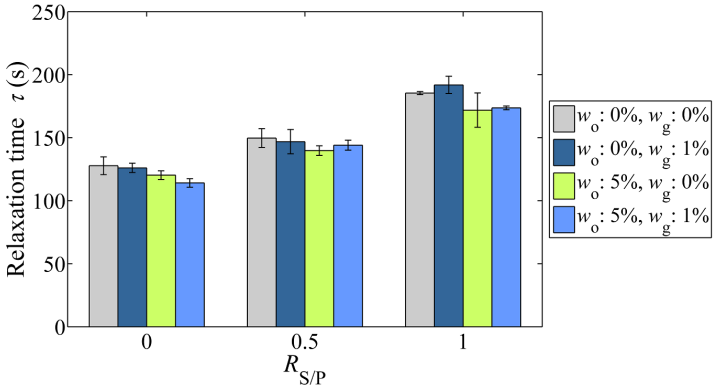

FIG. 10. The values of relaxation time constants τ for 12 PVC samples.

3.D. Friction Force in Needle Insertion

An example of the needle insertion force along the axial direction for six insertions to the PVC sample ($R_{S/P}$ of 0.5, w_o of 0, and w_g of 1%) is shown in Fig. 11. This needle insertion force profile was similar to that of silicone[11]. Seven regions (marked as Regions I-VII) were identified in the force profile. In Region I, the needle was inserted into the sample and punched out. There were four phases (marked as Phases I – IV) in Region I. In Phase I, the insertion force increased with time as the needle tip indented and deformed the soft sample until it reached the small peak value (of 0.15 N in the case shown in Fig. 11). In Phase II, the insertion force dropped slightly after the needle tip cut into the PVC surface. In Phase III, the insertion force increased due to the increase in the contact area and friction force between the needle and the PVC during the needle insertion until reaching the large peak value (of 1.13 N in this case). To this point, the needle insertion force is the summation of the cutting force and the friction force. In Phase IV, the insertion force dropped and remained relatively unchanged because the needle tip had punched out of the PVC sample. The contact surface area and friction force (about 1.05 N) between the needle and PVC sample remained the same in this Phase.

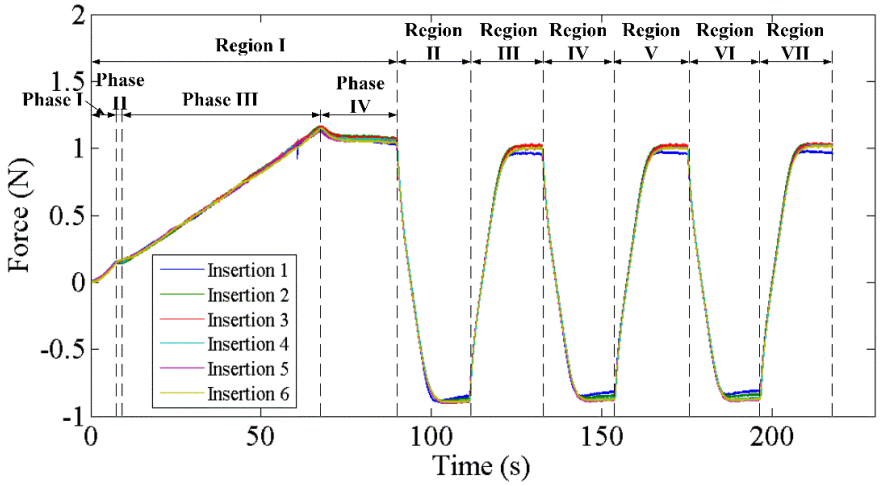

FIG. 11. An example of needle force of the six insertions into the PVC with $R_{S/P}$ of 0.5, w_o of 0, w_g of 1%.

In Regions II to VII, the needle was retracted and inserted three times. In Regions II, IV, and VI the needle was retracted by 20 mm with the tip still outside the sample. The force in these regions (about 0.87 N) was the friction force in the direction opposite to that in Region I. This force (0.87 N) was lower than that of Region I (1.05 N) due to the concave meniscus surface of the PVC phantom (as shown in Fig. 12(a)). As shown in Fig. 12(b), the sample

was more constrained in the advancing procedure than that in the retraction as shown in Fig. 12(c). Therefore, higher friction force on the needle surface was observed in Regions I (Phase IV), III, V, and VII. The friction force remained almost unchanged in the repeated needle insertions or retractions. It showed that the PVC samples were durable and could resist repeated needle insertions.

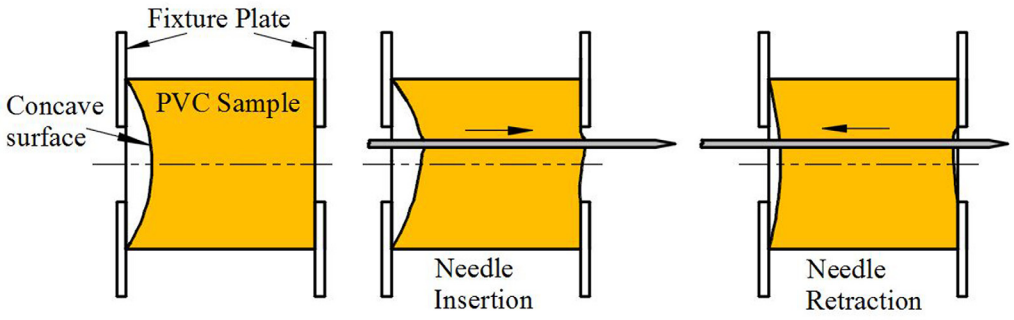

FIG. 12. Schematics to illustrate the difference in the insertion and retraction procedures: (a) before needle insertion, (b) needle insertion (Region III, V, and VII, in Fig. 11), and (c) needle retraction (Regions II, IV, and VI, in Fig. 11).

The average force of Phase IV in Region I was used to represent the friction force of the needle insertion. The friction force per unit length, denoted as f, was used as a parameter to compare the difference of the needle insertion property of the 12 PVC samples (as shown in Fig. 13). The error bars in Fig. 13 represent the standard deviation of the value of the three samples for each PVC material. PVC samples with w_o = 5% had about 50% lower f than those with w_o = 0. The f of the PVC samples in this study was in the range of 0.005 to 0.086 N/mm, which was similar to that of silicone with 20% to 40% mineral oil[11]. According to Table I, the f of the PVC samples was close to that of *ex vivo* animal liver.

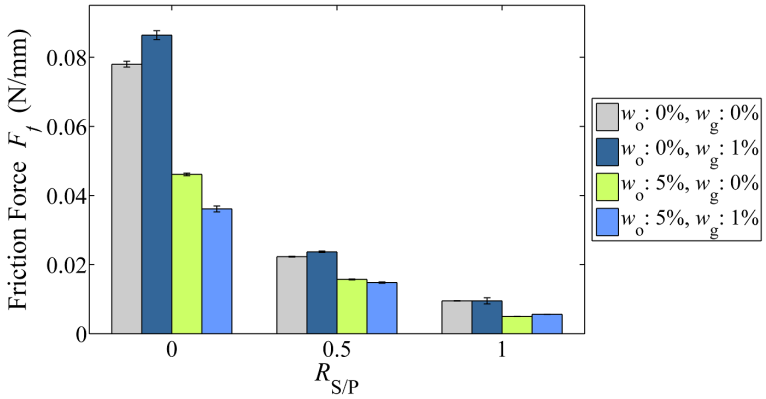

FIG. 13. Friction force per length f in needle insertion of 12 PVC samples.

3.E. Acoustic Properties of the PVC Samples

The speeds of sound, c, of the PVC samples are shown in Fig. 14. The error bars represent the standard deviation of the values of the three samples for each PVC material. The c decreased with the increase of $R_{S/P}$. The PVC samples with glass beads tended to have a slightly higher c than those without glass beads (except PVC sample with $R_{S/P}$ = 0, w_o = 5%, and w_g = 1%). As seen in Table I, most tissues in human and animals have speeds of sound around 1500 to 1600 m/s due to their water content. The speeds of sound in PVC samples of this paper were between 1390 and 1410 m/s, which has a gap with that of the normal tissue.

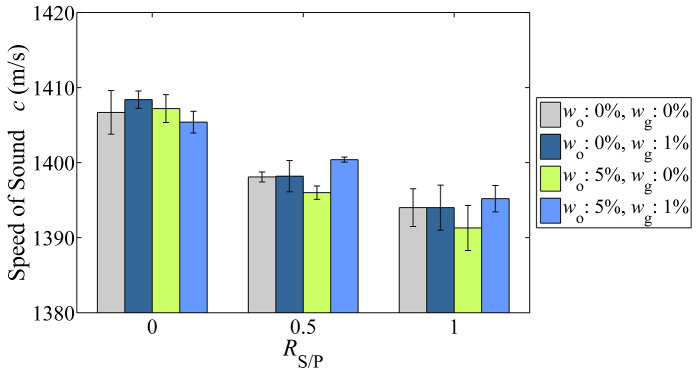

FIG. 14. Speeds of sound c of 12 PVC samples.

The acoustic attenuation coefficients, α, of the PVC samples are shown in Fig. 15. The error bars represent the standard deviation of the value of the three samples for each PVC material. The α decreased with the increasing $R_{S/P}$. The addition of glass beads raised α except in the PVC sample with $R_{S/P}$ = 0.5, w_o = 5%, and w_g = 1%. The

difference between samples with and without glass beads was large in samples with $R_{S/P} = 1$. According to Table I, α of PVC samples are slightly smaller than those of human brain and fat.

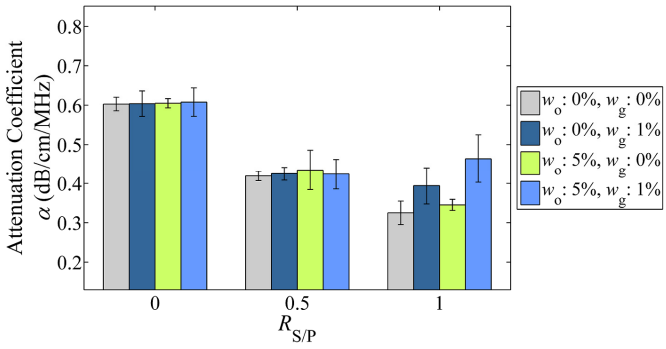

FIG. 15. Acoustic attenuation coefficients α of 12 PVC samples.

The addition of glass beads enhanced the acoustic scattering of the PVC samples for ultrasound imaging. Without glass beads, ultrasound images of PVC samples appear dark, as seen in Fig. 16(a). With glass beads, the ultrasound image generated speckles (see Fig. 16(b)), similar to those seen in human tissue ultrasound images.

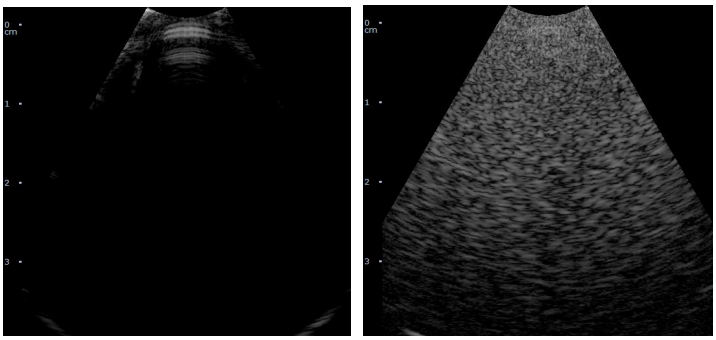

(a) (b)

FIG. 16. Ultrasound pictures of PVC samples with and without glass beads: (a) $R_{S/P} = 0$, $w_o = 0$, and $w_g = 0$ and (b) $R_{S/P} = 0$, $w_o = 0$, and $w_g = 1\%$.

3.F. Optical Clarity of the PVC Samples

The visible light transmittance of each PVC sample is shown in Fig. 17. The PVC samples with glass beads had 20% ~ 73% lower visible light transmittance than those without glass beads. However, the value of $R_{S/P}$ also

influenced the transmittance tending to increase transmittance with a larger $R_{S/P}$. Fig. 17 shows pictures of the clearest and the opaquest PVC samples atop a checkerboard background. The transparency of the other PVC samples was between these two extremes.

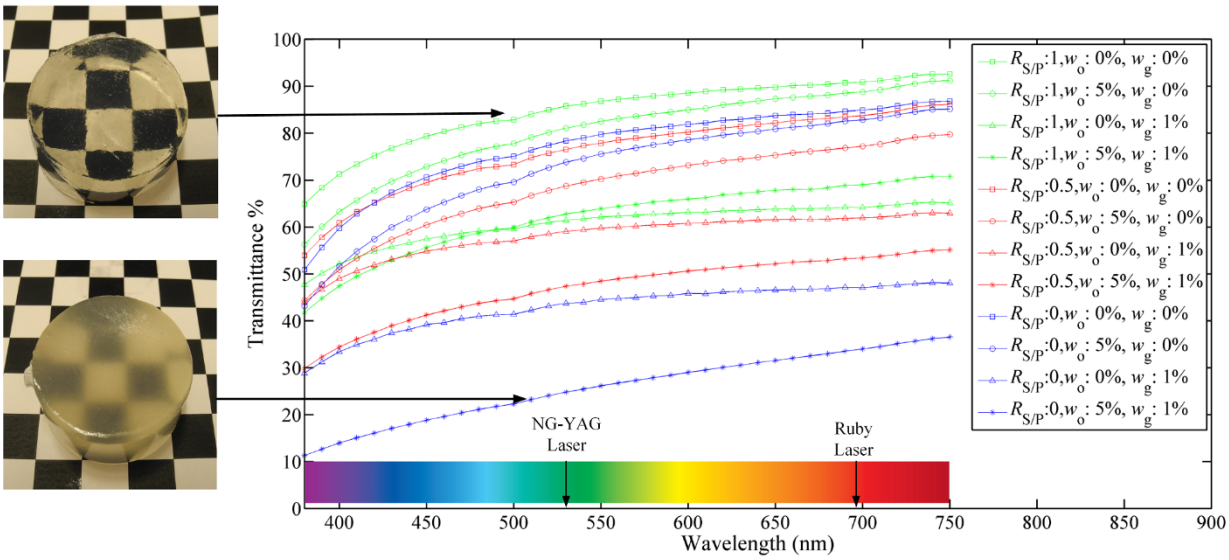

FIG. 17. Visible light transmittance in each PVC sample in the wavelength range from 380 nm to 750 nm.

To make the results more immediately practical, values of transmittance for the PVC samples for two common laser wavelengths are shown in Fig. 18. In this way, researchers could quantitatively design PVC material with desired optical transmittance given a desired wavelength of observation. These wavelengths are 532 nm (typically seen in NG-YAG lasers, widely used in PIV[111]) and 695 nm (seen in ruby lasers[112]). These two wavelengths are marked in Fig. 17. The transmittance at these two targeted wavelengths, 532 and 695 nm, are defined as $T_{\lambda 695}$ and $T_{\lambda 532}$, respectively. The transmittance of the samples increased with $R_{S/P}$, except for the samples with oil but without glass beads, because the softener can cross-link with the PVC polymer and make the sample more transparent. The sample with $R_{S/P} = 0.5$, $w_o = 5\%$, and $w_g = 0$ had smaller transmittance than that of the sample with $R_{S/P} = 0$, $w_o = 5\%$, and $w_g = 0$. It was attributed to the effect of oil on the cross-linking of the PVC polymers in the samples with $R_{S/P} = 0.5$. When the $R_{S/P}$ was larger, the effect of the oil was negligible and the transmittance was larger. Fig. 18 shows that the addition of glass beads lowered the transmittance by 20% ~ 73%. In the samples with $R_{S/P} = 0$, the drop of transmittance by the glass beads were larger than those of the sample with softener. It was because the softener

could increase the transparency of the sample and weaken the negative effect of the glass beads on the transmittance. The significance of the three factors on $T_{\lambda 695}$ and $T_{\lambda 532}$ were analyzed in Section IV.

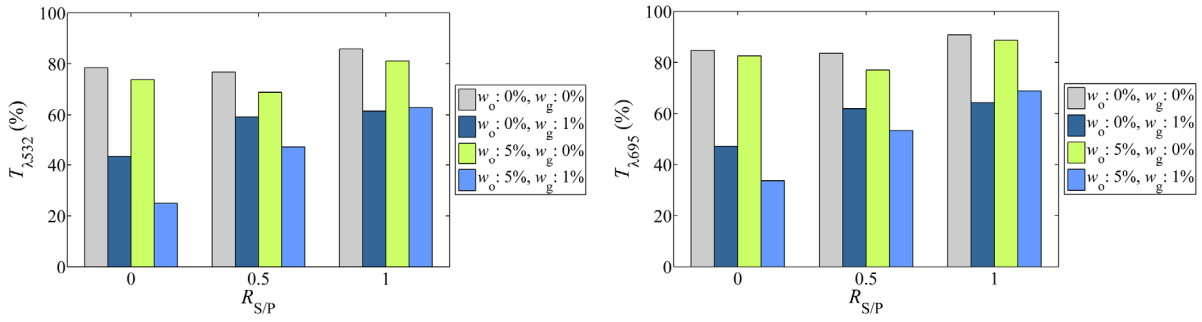

(a) (b)

FIG. 18. Transmittance of PVC samples at different wavelength of two lasers: (a) 532 nm and (b) 695 nm.

3.G. MRI Time Constants T_1 and T_2 of PVC Samples

A representative image set, a typical region of interest, and T_1 or T_2 maps of the sample with $R_{S/P} = 1$, $w_o = 0$, and $w_g = 1\%$ are shown in Fig. 19. Summary data (mean ± standard deviation) of T_1 and T_2 values of the PVC samples are shown in Figs. 20(a) and (b). The error bars represent the standard deviation of the value of the three samples for each PVC material. Ambient temperature near to the sample fluctuated minimally across all acquisitions (16.6 ± 0.4 °C). T_1 values varied about 9% across all samples (mean 438 ms; range 421 to 461 ms), with the mean of the fitting parameter accounting for potential incomplete relaxation (a) being 0.87 ± 0.04. T_2 values varied about 37% (mean 25 ms; range 21 to 29 ms). At the same high field strength (7 T) as that in this paper, the T_2 of fat was about 31 to 40 ms[113]; the T_1 of the white matter was 1220 ms[114]; the T_1 and T_2 of lymph nodes are 994 ms and 32 ms[115]. The T_1 and T_2 of the PVC samples are all lower than real tissue. $R_{S/P}$ had the greatest effect on T_1 and T_2. Both time constants increased with increasing $R_{S/P}$. Mineral oil had no clear effect on T_1 or T_2 while the addition of glass beads tended to slightly lower T_2.

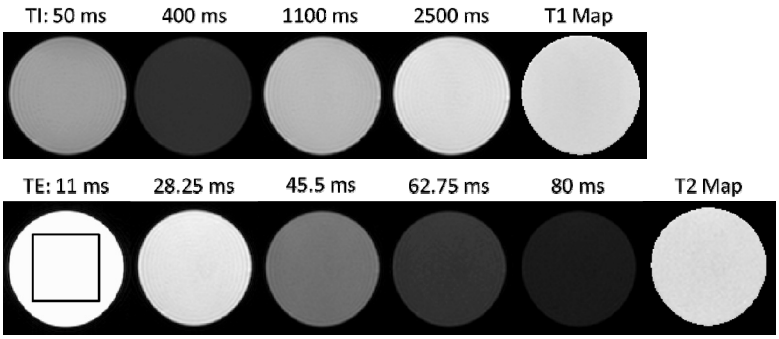

FIG. 19. Representative T_1 and T_2 images with resulting time constant maps. (*TI* = inversion time and *TE* = echo time)

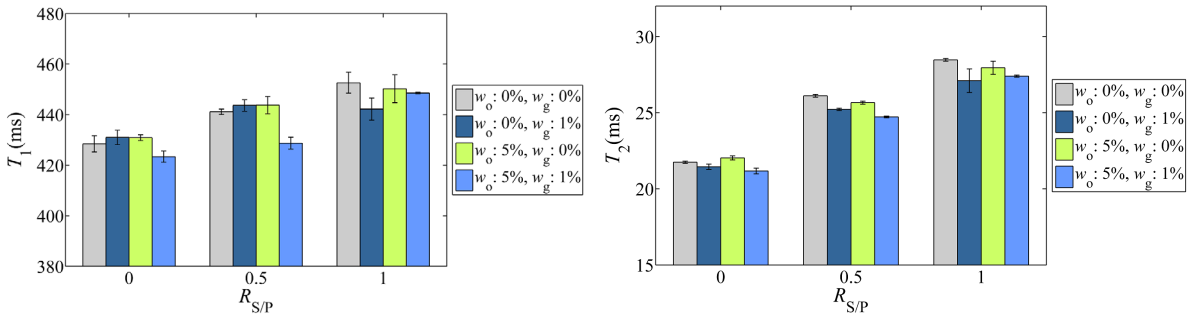

(a) (b)

FIG. 20. MRI time constants of 12 PVC samples: (a) T_1 and (b) T_2.

Although this work was performed at a higher field strength (7.0 T) than that which is approved for typical clinical use, it was the same field strength at which novel research is currently performed in humans[113–115]. Due to the unknowns related to the anatomy or physiology of interest, along with those associated with a newer field strength, this type of research at higher field strength was thought to benefit the most from the use of tissue-mimicking materials and phantoms to validate MRI techniques, including but not limited to pulse sequence and RF design. The only notable difference here was that this work was performed on a small bore system.

For T_1 measurements, the parameter (a) calculated from fitting suggested we did not use a repetition time long enough to allow for complete relaxation of spins (a = 0.87 vs. 1). This would result in a slight under estimation of T_1. However, the comparisons of sample content with respect to T_1 and T_2 time constants made here were performed with data acquired with imaging conditions being nearly constant, including temperature, which has a known influence on T_1[109].

4. Regression Model of the Mechanical and Imaging Properties of PVC

4.A. Factorial Analysis

The factorial analysis results of the main effects and two-way interactions of three factors ($R_{S/P}$, w_o, and w_g) on the elastic modulus (E), hardness (H), viscoelastic stress relaxation time constant (τ), needle insertion friction force (f), speed of sound (c), acoustic attenuation (α), MRI time constants (T_1 and T_2), transmittance at 695nm ($T_{\lambda 695}$), and 532 nm ($T_{\lambda 532}$) are summarized in Table III. Significant factors and interactions ($p \leq 0.05$) are marked with an asterisk (*). The $R_{S/P}$ had statistically significant effect on all properties of the PVC except $T_{\lambda 695}$ and $T_{\lambda 532}$; w_o had statistically significant effect on E, H, τ and f; and w_g had statistically significant effect on E, H, T_2, $T_{\lambda 695}$, and $T_{\lambda 532}$. The interaction of $R_{S/P}$ and w_o (denoted as $R_{S/P}$ * w_o in Table III) had statistically significant effect on E and f. The interaction of $R_{S/P}$ and w_g was statistically significant to E and H. The interaction of w_o and w_g only had statistically significant effect on f. Based on the factorial analysis results in Table III, regression equations of all properties tested in this paper were developed using the Minitab® with the corresponding statically significant factors and interactions. Since the p value of w_g (0.053) to T_1 is very close to 0.05, w_g was added to the regression equation of T_1. Although $R_{S/P}$ is a little larger than 0.05 for $T_{\lambda 695}$ and $T_{\lambda 532}$, we found that $R_{S/P}$ greatly affected the transparency of PVC samples. Therefore, $R_{S/P}$ was added to the regression equations for $T_{\lambda 695}$ and $T_{\lambda 532}$.

TABLE III. The factorial analysis of the three factors on PVC mechanical and imaging properties.

Factor	*p* value									
	Elastic modulus E	Hardness H	Stress relaxation time constant τ	Friction force f	Speed of Sound c	Attenuation α	MRI Relaxation Time T_1	MRI Relaxation Time T_2	Transmittance $T_{\lambda 695}$	Transmittance $T_{\lambda 532}$
$R_{S/P}$	<0.001*	<0.001*	<0.001*	<0.001*	<0.001*	<0.001*	<0.001*	<0.001*	0.074	0.076
w_o	<0.001*	<0.001*	0.021*	<0.001*	0.480	0.380	0.106	0.236	0.217	0.118
w_g	0.007*	0.098	0.933	0.396	0.120	0.146	0.053	<0.001*	0.008*	0.011*
$R_{S/P} * w_o$	0.007*	0.060	0.666	<0.001*	0.816	0.662	0.081	0.456	0.435	0.470
$R_{S/P} * w_g$	0.046*	0.008*	0.754	0.757	0.509	0.117	0.739	0.584	0.132	0.142
$w_o * w_g$	0.309	0.696	0.948	<0.001*	0.367	0.774	0.280	0.834	0.712	0.566

(* statistically significant, $p \leq 0.05$)

4.B. Regression Model

The regression equations and their R^2 values based on our experiments are listed in Table IV. The statistically significant factors and interactions were included in the regression equations. The $R_{S/P}^2$ term was added to improve accuracy of the regression model. For example, the regression equation of H included the statistically significant factors $R_{S/P}$ and w_o, the interaction $R_{S/P}$ * w_g, and the $R_{S/P}^2$. The ranges of the input parameters were $0 < R_{S/P} \leq 1$, $0 < w_o \leq 5\%$, and $0 < w_g \leq 1\%$ and output parameters ranges in the regression model are listed in Table IV.

TABLE IV. The regression equations of E, H, τ, f, c, α, T_1, T_2, $T_{\lambda 695}$, and $T_{\lambda 532}$.

Regression Equation	R^2	Applicable range
$E(\text{kPa}) = 45.5 - 78R_{S/P} - 75.7w_o - 218w_g + 63.6R_{S/P}w_o + 216R_{S/P}w_g + 39.6R_{S/P}^2$	0.99	6 − 45
$H = 50.9 - 63.6R_{S/P} - 65.6w_o - 13.3R_{S/P}w_g + 21.5R_{S/P}^2$	0.99	6 − 51
$\tau(\text{s}) = 125.3 + 58.7R_{S/P} - 214w_o$	0.83	114.1 – 191.9
$f(\text{N/mm}) = 0.08 - 0.13R_{S/P} - 0.69w_0 + 0.74R_{S/P}w_o - 7.18w_ow_g + 0.062R_{S/P}^2$	0.97	0.005 − 0.086
$c(\text{m/s}) = 1407 - 21.7R_{S/P} + 8.39R_{S/P}^2$	0.84	1393 − 1407
$\alpha(\text{dB/cm/MHz}) = 0.61 - 0.5R_{S/P} + 0.27R_{S/P}^2$	0.72	0.38 – 0.61
$T_1(\text{ms}) = 430 + 20.0R_{S/P} - 393w_g$	0.67	426.3 – 450.2
$T_2(\text{ms}) = 22.3 + 6.13R_{S/P} - 81.9w_g$	0.97	21.5 – 28.4
$T_{\lambda 695}(\%) = 76.5 + 16.1R_{S/P} - 2970w_g$	0.88	46.8 − 92.6
$T_{\lambda 532}(\%) = 68.7 + 17.6R_{S/P} - 2760w_g$	0.83	41.1 − 86.3

5. Application of Regression Model to Design the PVC with Targeted Mechanical Properties and the Experimental Validation

The mechanical properties of the PVC samples have large ranges and close to those of tissues according to Table I. However, the medical imaging properties have a small range and a discrepancy with real tissue. Therefore, the regression models of the mechanical properties can be used to design the material while those of medical imaging properties could still be used to forecast the properties of PVC samples with the $R_{S/P}$, w_o, and w_g in the ranges of this study.

By specifying values for any three of the four parameters (E, H, τ, and f) within the range of regression model, the composition of PVC ($R_{S/P}$, w_o, and w_g) could be obtained. For example, given E = 22.0 kPa, τ = 139.3 s, and f = 0.0318 N/mm, the regression model calculated $R_{S/P}$ = 0.33, w_o = 2.5%, and w_g = 0.5%. The fourth mechanical property H and medical imaging properties (c, α, T_1, T_2, $T_{\lambda 695}$, and $T_{\lambda 532}$) could be obtained with the regression equations.

To validate the accuracy of the regression model, a PVC sample with $R_{S/P}$ = 0.33, w_o = 2.5%, and w_g = 0.5% was fabricated and the mechanical and medical imaging properties of the new sample were tested with experiments and compared to the calculated values from the regression equations. As shown in Table V, except f, the error of each property is lower than 5%. The error of f is 14.8% because the value of f is affected by other mechanical properties of the PVC sample, such as E and τ. The errors of other properties aggregated to make the error of f very large. This example demonstrates the feasibility of applying the regression model to find the composition of $R_{S/P}$, w_o, and w_g and design a PVC material with desired mechanical properties. The medical imaging properties of PVC material could be forecasted accurately.

TABLE V. Validation results of the PVC materials with $R_{S/P}$ of 0.33, w_o of 2.5%, and w_g of 0.5%.

	Calculated Value	Experimental Results	Error	Max allowable error
E (kPa)	22.0	22.8	3.4%	86.7%
H	30.6	30.3	0.98%	88.2%
τ (s)	139.3	134.3	4%	68.2%
f (N/mm)	0.0318	0.0365	14.8%	94.2%
c (m/s)	1400	1408	0.6%	1%
α (dB/cm/MHz)	0.47	0.45	4.0%	37.7%
T_1 (ms)	434.8	444	2.1%	5.3%
T_2 (ms)	23.9	24	0.4%	24.3%
$T_{\lambda 695}$ (%)	67	66.3	1.0%	49.4%
$T_{\lambda 503}$ (%)	60.7	60.5	0.3%	52.3%

(The maximum allowable error is the ratio of the difference between maximum and minimum value normalized to the maximum value in the applicable range of the regression equation.)

6. Conclusions

The procedure of applying a regression model to find the formulation of PVC ($R_{S/P}$, w_o, and w_g) to achieve targeted mechanical properties was demonstrated and validated experimentally. Based on this approach, PVC phantom tissues for clinical simulators or medical research devices could be designed with desired mechanical

properties and an appropriate composition of PVC can be identified using the regression model. The medical imaging properties of the PVC samples have narrow ranges and commonly are not close enough to those of real tissues. The regression models of medical imaging properties were able to predict the value of these properties of the PVC sample with known composition.

There are several limitations of the PVC material in this study. The mechanical and imaging properties of the PVC phantom material will gradually change over time. The long-term stability and effects of properties of the PVC phantom material require further study. This PVC material is not suitable to mimic the brain. Since the speeds of sound of the PVC samples in this paper are lower than that of normal tissue, other additives which can increase the speed of sound will be added. In addition, more research on the echogenicity of the phantom is also needed.

Acknowledgements

This research work is sponsored by the Nation Science Foundation (NSF) Award CMMI 1266063 and the Chinese Scholarship Council.

The authors have no relevant conflicts of interest to disclose.

References

[1] J. Dankelman, "Surgical simulator design and development.," World J. Surg. **32**(2), 149–155 (2008).

[2] K.J. Domuracki, C.J. Moule, H. Owen, G. Kostandoff, and J.L. Plummer, "Learning on a simulator does transfer to clinical practice.," Resuscitation **80**(3), 346–349 (2009).

[3] A. Liu, F. Tendick, K. Cleary, and C. Kaufmann, "A survey of surgical simulation: applications, technology, and education," Presence Teleoperators Virtual Environ. **12**(6), 599–614 (2003).

[4] M. Srinivasan, J.C. Hwang, D. West, and P.M. Yellowlees, "Assessment of clinical skills using simulator technologies.," Acad. Psychiatry **30**(6), 505–515 (2006).

[5] M.O. Culjat, D. Goldenberg, P. Tewari, and R.S. Singh, "A review of tissue substitutes for ultrasound imaging.," Ultrasound Med. Biol. **36**(6), 861–873 (2010).

[6] R. Cao, Z. Huang, T. Varghese, and G. Nabi, "Tissue mimicking materials for the detection of prostate cancer using shear wave elastography: A validation study.," Med. Phys. **40**(2), 022903 (2013).

[7] T. Yoshida, K. Tanaka, T. Kondo, K. Yasukawa, N. Miyamoto, M. Taniguchi, and Y. Shikinami, "Tissue-mimicking materials using segmented polyurethane gel and their acoustic properties," Jpn. J. Appl. Phys. **51**(7S), 07GF17 (2012).

[8] E.L. Madsen, M.A. Hobson, H. Shi, T. Varghese, and G.R. Frank, "Tissue-mimicking agar/gelatin materials for use in heterogeneous elastography phantoms.," Phys. Med. Biol. **50**(23), 5597–5618 (2005).

[9] S.J.-S. Chen, P. Hellier, M. Marchal, J.-Y. Gauvrit, R. Carpentier, X. Morandi, and D.L. Collins, "An anthropomorphic polyvinyl alcohol brain phantom based on Colin27 for use in multimodal imaging.," Med. Phys. **39**(1), 554–561 (2012).

[10] M. Solanki and V. Raja, "Haptic based augmented reality simulator for training clinical breast examination," in *Biomed. Eng. Sci. (IECBES), 2010 IEEE EMBS Conf.*(2010), pp. 265–269.

[11] Y. Wang, B.L. Tai, H. Yu, and A.J. Shih, "Silicone-based tissue-mimicking phantom for needle insertionsimulation," J. Med. Device. **8**(2), 21001 (2014).

[12] J. Oudry, C. Bastard, V. Miette, R. Willinger, and L. Sandrin, "Copolymer-in-oil phantom materials for elastography.," Ultrasound Med. Biol. **35**(7), 1185–1197 (2009).

[13] A.S. Kashif, T.F. Lotz, M.D. McGarry, A.J. Pattison, and J.G. Chase, "Silicone breast phantoms for elastographic imaging evaluation.," Med. Phys. **40**(6), 63503 (2013).

[14] J. Fromageau, J.-L. Gennisson, C. Schmitt, R.L. Maurice, R. Mongrain, and G. Cloutier, "Estimation of polyvinyl alcohol cryogel mechanical properties with four ultrasound elastography methods and comparison with gold standard testings.," IEEE Trans. Ultrason. Ferroelectr. Freq. Control **54**(3), 498–509 (2007).

[15] M.M. Nguyen, S. Zhou, J.-L. Robert, V. Shamdasani, and H. Xie, "Development of oil-in-gelatin phantoms for viscoelasticity measurement in ultrasound shear wave elastography.," Ultrasound Med. Biol. **40**(1), 168–176 (2014).

[16] N. Hungr, J.-A. Long, V. Beix, and J. Troccaz, "A realistic deformable prostate phantom for multimodal imaging and needle-insertion procedures.," Med. Phys. **39**(4), 2031–2041 (2012).

[17] M.K. Chmarra, R. Hansen, R. Marvik, and T. Lango, "Multimodal phantom of liver tissue.," PLoS One **8**(5), e64180 (2013).

[18] D.W. Rickey, P.A. Picot, D.A. Christopher, and A. Fenster, "A wall-less vessel phantom for doppler ultrasound studies," Ultrasound Med. Biol. **21**(9), 1163–1176 (1995).

[19] C.L. de Korte, E.I. Cespedes, A.F.W. van der Steen, and C.T. Lancee, "Intravascular elasticity imaging using ultrasound: Feasibility studies in phantoms," Ultrasound Med. Biol. **23**(5), 735–746 (1997).

[20] E.L. Madsen, E. Kelly-Fry, and G.R. Frank, "Anthrpomorphic phantoms for assessing systems used in ultrasound imaging of the compressed breast," Ultrasound Med. Biol. **14**(1), 183–201 (1988).

[21] I. Mano, H. Goshima, M. Nambu, and M. Iio, "New polyvinyl alcohol gel material for MRI phantoms.," Magn. Reson. Med. **3**(6), 921–926 (1986).

[22] N.J. Lawson and J. Wu, "Three-dimensional particle image velocimetry: experimental error analysis of a digital angular stereoscopic system," Meas. Sci. Technol. **8**(12), 1455–1464 (1997).

[23] R.K. Chen and A.J. Shih, "Multi-modality gellan gum-based tissue-mimicking phantom with targeted mechanical, electrical, and thermal properties.," Phys. Med. Biol. **58**(16), 5511–5525 (2013).

[24] B.W. Pogue and M.S. Patterson, "Review of tissue simulating phantoms for optical spectroscopy, imaging and dosimetry.," J. Biomed. Opt. **11**(4), 41102 (2006).

[25] G.M. Spirou, A.A. Oraevsky, I.A. Vitkin, and W.M. Whelan, "Optical and acoustic properties at 1064 nm of polyvinyl chloride-plastisol for use as a tissue phantom in biomedical optoacoustics.," Phys. Med. Biol. **50**(14), N141–53 (2005).

[26] I.M. de Carvalho, R.L.Q. Basto, A.F.C. Infantosi, M.A. von Krüger, and W.C.A. Pereira, "Breast ultrasound imaging phantom to mimic malign lesion characteristics," Phys. Procedia **3**(1), 421–426 (2010).

[27] J.K. Tsou, J. Liu, A.I. Barakat, and M.F. Insana, "Role of ultrasonic shear rate estimation errors in assessing inflammatory response and vascular risk.," Ultrasound Med. Biol. **34**(6), 963–972 (2008).

[28] L. Maggi, G. Cortela, V. Krüger，M，A, Negreira，C, and W.C. de Albuquerque Pereira, "Ultrasonic attenuation and speed in phantoms made of PVCP and evaluation of acoustic and thermal properties of ultrasonic phantoms made of polyvinyl chloride plastisol (PVCP)," in *IWBBIO 2013. Proc.*(2013), pp. 233–241.

[29] H. Tanoue, Y. Hagiwara, K. Kobayashi, and Y. Saijo, "Ultrasonic tissue characterization of prostate biopsy tissues by ultrasound speed microscope," Proc. Annu. Int. Conf. IEEE Eng. Med. Biol. Soc. EMBS 8499–8502 (2011).

[30] M.O. Woods and C.A. Miles, "Ultrasound speed and attenuation in homogenates of bovine skeletal muscle," Ultrasonics **24**(5), 260–266 (1986).

[31] F.W. Kremkau, R.W. Barnes, and C.P. McGraw, "Ultrasonic attenuation and propagation speed in normal human brain," J. Acoust. Soc. Am. **70**(1), 29–38 (1981).

[32] J.C. Bamber, "Ultrasonic attenuation in fress human tissues," Ultrasonics 187–188 (1981).

[33] D.L. Folds, "Speed of sound and transmission loss in silicone rubbers at ultrasonic frequencies," J. Acoust. Soc. Am. **56**(4), (1974).

[34] A. Ashead and S.M. Lindsay, "Brillouin scattering from polyurethane gels," Polymer (Guildf). **23**, 1884–1888 (1982).

[35] R.L. Cook and D. Kendrick, "Speed of sound of six PRC polyurethane materials as a function of temperature," J. Acoust. Soc. Am. **70**(2), 639–640 (1981).

[36] K.A. Ross and M.G. Scanlon, "Analysis of the elastic modulus of agar gel by indentation," J. Texture Stud. **30**(1), 17–27 (1999).

[37] V.T. Nayar, J.D. Weiland, C.S. Nelson, and A.M. Hodge, "Elastic and viscoelastic characterization of agar.," J. Mech. Behav. Biomed. Mater. **7**, 60–68 (2012).

[38] T.Z. Pavan, E.L. Madsen, G.R. Frank, A. Adilton O Carneiro, and T.J. Hall, "Nonlinear elastic behavior of phantom materials for elastography.," Phys. Med. Biol. **55**(9), 2679–2692 (2010).

[39] C. Sun, S.D. Pye, J.E. Browne, A. Janeczko, B. Ellis, M.B. Butler, V. Sboros, A.J.W. Thomson, M.P. Brewin, C.H. Earnshaw, and C.M. Moran, "The speed of sound and attenuation of an IEC agar-based tissue-mimicking material for high frequency ultrasound applications.," Ultrasound Med. Biol. **38**(7), 1262–1270 (2012).

[40] K. Manickam, R.R. Machireddy, and S. Seshadri, "Characterization of biomechanical properties of agar based tissue mimicking phantoms for ultrasound stiffness imaging techniques.," J. Mech. Behav. Biomed. Mater. **35**, 132–143 (2014).

[41] R.F. Smith, B.K. Rutt, and D.W. Holdsworth, "Anthropomorphic carotid bifurcation phantom for MRI applications.," J. Magn. Reson. Imaging **10**(4), 533–544 (1999).

[42] R. Mathur-De Vre, R. Grimee, F. Parmentier, and J. Binet, "The use of agar gel as a basic reference material for calibrating relaxation times and imaging parameters.," Magn. Reson. Med. **2**(2), 176–179 (1985).

[43] E. Raphael, C.O. Avellaneda, B. Manzolli, and A. Pawlicka, "Agar-based films for application as polymer electrolytes," Electrochim. Acta **55**(4), 1455–1459 (2010).

[44] B. Luo, R. Yang, P. Ying, M. Awad, M. Choti, and R. Taylor, "Elasticity and echogenicity analysis of agarose phantoms mimicking liver tumors," in *Bioeng. Conf. 2006. Proc. IEEE 32nd Annu. Northeast*(2006), pp. 81–82.

[45] V. Normand, D.L. Lootens, E. Amici, K.P. Plucknett, and P. Aymard, "New insight into agarose gel mechanical properties.," Biomacromolecules **1**(4), 730–738 (2000).

[46] S.A. Lopez-Haro, C.J. Trujillo, A. Vera, and L. Leija, "An agarose based phantom embedded in an in vitro liver tissue to simulate tumors: First experience," in *Heal. Care Exch. (PAHCE), 2011 Pan Am.*(2011), pp. 233–236.

[47] S.A. Lopez-Haro, I. Bazan-Trujillo, L. Leija-Salas, and A. Vera-Hernandez, "Ultrasound propagation speed measurement of mimicking soft tissue phantoms based on agarose in the range of 25 ℃ and 50 ℃," in *Electr. Eng. Comput. Sci. Autom. Control. 2008. CCE 2008. 5th Int. Conf.*(2008), pp. 192–195.

[48] H.I. Litt and A.S. Brody, "BaSO4-loaded agarose: a construction material for multimodality imaging phantoms.," Acad. Radiol. **8**(5), 377–383 (2001).

[49] M.D. Mitchell, H.L. Kundel, L. Axel, and P.M. Joseph, "Agarose as a tissue equivalent phantom material for NMR imaging.," Magn. Reson. Imaging **4**(3), 263–266 (1986).

[50] M. Penders, S. Nilsson, L. Piculell, and B. Lindman, "Clouding and diffusion of nonionic surfactants in agarose gels and solutions," J. Phys. Chem. **97**(43), 11332–11338 (1993).

[51] X. Zhang, B. Qiang, and J. Greenleaf, "Comparison of the surface wave method and the indentation method for measuring the elasticity of gelatin phantoms of different concentrations," Ultrasonics **51**(2), 157–164 (2011).

[52] R.J. Roesthuis, Y.R.J. van Veen, A. Jahya, and S. Misra, "Mechanics of needle-tissue interaction," in *Intell. Robot. Syst. (IROS), 2011 IEEE/RSJ Int. Conf.*(2011), pp. 2557–2563.

[53] J.C. Blechinger, E.L. Madsen, and G.R. Frank, "Tissue-mimicking gelatin-agar gels for use in magnetic resonance imaging phantoms.," Med. Phys. **15**(4), 629–636 (1988).

[54] S. Smitha, P. Shajesh, P. Mukundan, T.D.R. Nair, and K.G.K. Warrier, "Synthesis of biocompatible hydrophobic silica-gelatin nano-hybrid by sol-gel process.," Colloids Surf. B. Biointerfaces **55**(1), 38–43 (2007).

[55] D.F. Coutinho, S. V Sant, H. Shin, J.T. Oliveira, M.E. Gomes, N.M. Neves, A. Khademhosseini, and R.L. Reis, "Modified gellan gum hydrogels with tunable physical and mechanical properties.," Biomaterials **31**(29), 7494–7502 (2010).

[56] A. Asadian, M.R. Kermani, and R. V. Patel, "A compact dynamic force model for needle-tissue interaction," in *2010 Annu. Int. Conf. IEEE Eng. Med. Biol. Soc. EMBC'10*(2010), pp. 2292–2295.

[57] A. Asadian, R. V. Patel, and M.R. Kermani, "Compensation for relative velocity between needle and soft tissue for friction modeling in needle insertion," in *Proc. Annu. Int. Conf. IEEE Eng. Med. Biol. Soc. EMBS*(2012), pp. 960–963.

[58] R.L. King, Y. Liu, S. Maruvada, B.A. Herman, K.A. Wear, and G.R. Harris, "Development and characterization of a tissue-mimicking material for high-intensity focused ultrasound.," IEEE Trans. Ultrason. Ferroelectr. Freq. Control **58**(7), 1397–1405 (2011).

[59] K.J.M. Surry, H.J.B. Austin, A. Fenster, and T.M. Peters, "Poly(vinyl alcohol) cryogel phantoms for use in ultrasound and MR imaging.," Phys. Med. Biol. **49**(24), 5529–5546 (2004).

[60] W. Xia, D. Piras, M. Heijblom, W. Steenbergen, T.G. van Leeuwen, and S. Manohar, "Poly(vinyl alcohol) gels as photoacoustic breast phantoms revisited.," J. Biomed. Opt. **16**(7), 75002 (2011).

[61] K.C. Chu and B.K. Rutt, "Polyvinyl alcohol cryogel: an ideal phantom material for MR studies of arterial flow and elasticity.," Magn. Reson. Med. **37**(2), 314–319 (1997).

[62] Z. Wang, B. Huang, X. Qin, X. Zhang, P. Wang, J. Wei, J. Zhan, X. Jing, H. Liu, Z. Xu, H. Cheng, X. Wang, and Z. Zheng, "Growth of high transmittance vertical aligned ZnO nanorod arrays with polyvinyl alcohol by hydrothermal method," Mater. Lett. **63**(1), 130–132 (2009).

[63] M. Kita, Y. Ogura, Y. Honda, S.H. Hyon, W. 2nd Cha, and Y. Ikada, "Evaluation of polyvinyl alcohol hydrogel as a soft contact lens material.," Graefes Arch. Clin. Exp. Ophthalmol. **228**(6), 533–537 (1990).

[64] S. Misra, K.B. Reed, B.W. Schafer, K.T. Ramesh, and A.M. Okamura, "Mechanics of flexible needles robotically steered through soft tissue.," Int. J. Rob. Res. **29**(13), 1640–1660 (2010).

[65] M. Carbone, S. Condino, L. Mattei, P. Forte, V. Ferrari, and F. Mosca, "Anthropomorphic ultrasound elastography phantoms - characterization of silicone materials to build breast elastography phantoms.," in *Annu. Int. Conf. IEEE Eng. Med. Biol. Soc.*(United States, 2012), pp. 492–494.

[66] C.L. Cheung, T. Looi, J. Drake, and P.C.W. Kim, "Magnetic resonance imaging properties of multimodality anthropomorphic silicone rubber phantoms for validating surgical robots and image guided therapy systems," in *Proc. SPIE 8316, Med. Imaging 2012 Image-Guided Proced. Robot. Interv. Model.*(2012), p. 83161X–83161X–9.

[67] D.C. Goldstein, H.L. Kundel, M.E. Daube-Witherspoon, L.E. Thibault, and E.J. Goldstein, "A silicone gel phantom suitable for multimodality imaging.," Invest. Radiol. **22**(2), 153–157 (1987).

[68] G.M. Bernacca, B. O'Connor, D.F. Williams, and D.J. Wheatley, "Hydrodynamic function of polyurethane prosthetic heart valves: Influences of Young's modulus and leaflet thickness," Biomaterials **23**(1), 45–50 (2002).

[69] B.-S. Chiou and P.E. Schoen, "Effects of crosslinking on thermal and mechanical properties of polyurethanes," J. Appl. Polym. Sci. **83**(1), 212–223 (2002).

[70] D. Fuerst, D. Stephan, P. Augat, and A. Schrempf, "Foam phantom development for artificial vertebrae used for surgical training.," Annu. Int. Conf. IEEE Eng. Med. Biol. Soc. 5773–5776 (2012).

[71] W.D. D'Souza, E.L. Madsen, O. Unal, K.K. Vigen, G.R. Frank, and B.R. Thomadsen, "Tissue mimicking materials for a multi-imaging modality prostate phantom.," Med. Phys. **28**(4), 688–700 (2001).

[72] K. Yasukawa, T. Kunisue, K. Tsuta, Y. Shikinami, and T. Kondo, "An ultrasound phantom with long-term stability using a new biomimic soft gel material," in *Ultrason. Symp. 2007. IEEE*(2007), pp. 2501–2502.

[73] E.L. Madsen, W.D. D'Souza, and G.R. Frank, Multi-imaging modality tissue mimicking materials for imaging phantoms, US6635486, 2001.

[74] S. Zhou, L. Wu, J. Sun, and W. Shen, "The change of the properties of acrylic-based polyurethane via addition of nano-silica," Prog. Org. Coatings **45**(1), 33–42 (2002).

[75] M.M. Jalili, S. Moradian, H. Dastmalchian, and A. Karbasi, "Investigating the variations in properties of 2-pack polyurethane clear coat through separate incorporation of hydrophilic and hydrophobic nano-silica," Prog. Org. Coatings **59**(1), 81–87 (2007).

[76] X. Liang, A.L. Oldenburg, V. Crecea, S. Kalyanam, M.F. Insana, and S.A. Boppart, "Modeling and measurement of tissue elastic moduli using optical coherence elastography," in *Proc. SPIE 6858, Opt. Tissue Eng. Regen. Med. II*(2008), pp. 685803–685808.

[77] V.P. Mathews, A.D. Elster, P.B. Barker, B.L. Buff, J.A. Haller, and C.M. Greven, "Intraocular silicone oil: in vitro and in vivo MR and CT characteristics.," AJNR. Am. J. Neuroradiol. **15**(2), 343–347 (1994).

[78] T.-K. Shih, C.-F. Chen, J.-R. Ho, and F.-T. Chuang, "Fabrication of PDMS (polydimethylsiloxane) microlens and diffuser using replica molding," Microelectron. Eng. **83**(11-12), 2499–2503 (2006).

[79] G.S. Rajan, G.S. Sur, J.E. Mark, D.W. Schaefer, and G. Beaucage, "Preparation and characterization of some unusually transparent poly(dimethylsiloxane) nanocomposites," J. Polym. Sci. Part B Polym. Phys. **41**(16), 1897–1901 (2003).

[80] E.J. Chen, J. Novakofski, W. Kenneth Jenkins, and W.D. O'Brien, "Young's modulus measurements of soft tissues with application to elasticity imaging," IEEE Trans. Ultrason. Ferroelectr. Freq. Control **43**(1), 191–194 (1996).

[81] W.C. Yeh, P.C. Li, Y.M. Jeng, H.C. Hsu, P.L. Kuo, M.L. Li, P.M. Yang, and H.L. Po, "Elastic modulus measurements of human liver and correlation with pathology," Ultrasound Med. Biol. **28**(4), 467–474 (2002).

[82] Y. Kobayashi, T. Sato, and M.G. Fujie, "Modeling of friction force based on relative velocity between liver tissue and needle for needle insertion simulation plates needle," in *2009 Annu. Int. Conf. IEEE Eng. Med. Biol. Soc.*(Minneapolis, MN, 2009), pp. 5274–5278.

[83] A. Asadian, R. V. Patel, and M.R. Kermani, "Dynamics of translational friction in needle-tissue interaction during needle insertion," Ann. Biomed. Eng. **42**(1), 73–85 (2014).

[84] J.C. Bamber and C.R. Hill, "Ultrasonic attenuation and propagation speed in mammalian tissues as a function of temperature," Ultrasound Med. Biol. **5**(2), 149–157 (1979).

[85] J.C. Bamber and C.R. Hill, "Acoustic properties of normal and cancerous human liver-I. Dependence on pathological condition," Ultrasound Med. Biol. **7**(2), 121–133 (1981).

[86] R. Nyman, A. Ericsson, A. Hemmingsson, B. Jung, G. Sperber, and K.A. Thuomas, "T1, T2, and relative proton density at 0.35 T for spleen, liver, adipose tissue, and vertebral body: normal values," Magn. Reson. Med. **3**, 901–910 (1986).

[87] G.J. Stanisz, E.E. Odrobina, J. Pun, M. Escaravage, S.J. Graham, M.J. Bronskill, and R.M. Henkelman, "T1, T2 relaxation and magnetization transfer in tissue at 3T," Magn. Reson. Med. **54**(3), 507–512 (2005).

[88] Z. Taylor and K. Miller, "Reassessment of brain elasticity for analysis of biomechanisms of hydrocephalus," J. Biomech. **37**(8), 1263–1269 (2004).

[89] F. Casanova, P.R. Carney, and M. Sarntinoranont, "In vivo evaluation of needle force and friction stress during insertion at varying insertion speed into the brain," J. Neurosci. Methods **237**, 79–89 (2014).

[90] B. Fischl, D.H. Salat, A.J.W. Van Der Kouwe, N. Makris, F. Ségonne, B.T. Quinn, and A.M. Dale, "Sequence-independent segmentation of magnetic resonance images," Neuroimage **23**(SUPPL. 1), 69–84 (2004).

[91] J.T. Iivarinen, R.K. Korhonen, and J.S. Jurvelin, "Experimental and numerical analysis of soft tissue stiffness measurement using manual indentation device - significance of indentation geometry and soft tissue thickness," Ski. Res. Technol. **20**(3), 347–354 (2014).

[92] B.A. Bullen, F. Quaade, E. Olesen, and S.A. Lund, "Ultrasonic reflections used for measuring subcutaneous fat in humans," Hum. Biol. **37**(4), 375–384 (1965).

[93] R.L. Errabolu, C.M. Sehgal, R.C. Bahn, and J.F. Greenleaf, "Measurement of ultrasonic nonlinear parameter in excised fat tissues," Ultrasound Med. Biol. **14**(2), 137–146 (1988).

[94] R.L. Ehman, B.O. Kjos, H. Hricak, R.C. Brasch, and C.B. Higgins, "Relative intensity of abdominal organs in MR images," J. Comput. Assist. Tomogr. **9**(2), 315–319 (1985).

[95] B.C.W. Kot, Z.J. Zhang, A.W.C. Lee, V.Y.F. Leung, and S.N. Fu, "Elastic Modulus of Muscle and Tendon with Shear Wave Ultrasound Elastography: Variations with Different Technical Settings," PLoS One **7**(8), 1–7 (2012).

[96] Y. Fukushima and K. Naemura, "Estimation of the friction force during the needle insertion using the disturbance observer and the recursive least square," ROBOMECH J. **1**(1), 1–8 (2014).

[97] B.M. Ahn, J. Kim, L. Ian, K.H. Rha, and H.J. Kim, "Mechanical property characterization of prostate cancer using a minimally motorized indenter in an ex vivo indentation experiment," Urology **76**(4), 1007–1011 (2010).

[98] X. Wang, J. Wang, Y. Liu, H. Zong, X. Che, W. Zheng, F. Chen, Z. Zhu, D. Yang, and X. Song, "Alterations in mechanical properties are associated with prostate cancer progression.," Med. Oncol. **31**(3), 876 (2014).

[99] T. Podder, D. Clark, J. Sherman, D. Fuller, E. Messing, D. Rubens, J. Strang, R. Brasacchio, L. Liao, W.-S. Ng, and Y. Yu, "Vivo motion and force measurement of surgical needle intervention during prostate brachytherapy.," Med. Phys. **33**(8), 2915–2922 (2006).

[100] L. Kjaer, C. Thomsen, P. Iversen, and O. Henriksen, "In vivo estimation of relaxation processes in benign hyperplasia and carcinoma of the prostate gland by magnetic resonance imaging," Magn. Reson. Imaging **5**, 23–30 (1987).

[101] Montgometry D C, *"*Design and Analysis of Experiments*"* (John Wiley & Sons, New Jersey, 2008).

[102] H. Mehrabian and A. Samani, "Constrained hyperelastic parameters reconstruction of PVA (Polyvinyl Alcohol) phantom undergoing large deformation," in *Proc. SPIE Med. Imaging Vis. Image-Guided Proced. Model.*(Spie, 2009), p. 72612G–72612G–11.

[103] ASTM, *"*International standard test method for rubber property—durometer hardness ASTM Standard D2240-05*"* (West Conshohocken, 2015).

[104] B.J. Briscoe, K.S. Sebastian, and M.J. Adams, "The effect of indenter geometry on the elastic response to indentation," J. Phys. D. Appl. Phys. **27**(6), 1156–1162 (1999).

[105] D.J. Naylor, "Stresses in nearly incompressible materials by finite elements with application to the calculation of excess pore pressures," Int. J. Numer. Methods Eng. **8**(December 1973), (1974).

[106] Ferry J D, *"*Viscoelastic Properties of Polymers*"* (Wiley, New York, 1980).

[107] W. Xu and J.J. Kaufman, "Diffraction correction methods for insertion ultrasound attenuation estimation," IEEE Trans. Biomed. Eng. **40**(6), 563–570 (1993).

[108] K. Sharma, *"*Optics*"* (Academic Press, 2006).

[109] R.J. Dickinson, A.S. Hall, A.J. Hind, and I.R. Young, "Measurement of changes in tissue temperature using MR imaging," J. Comput. Assist. Tomogr. **10**(3), 468–472 (1986).

[110] Lakes R S, *"*Viscoelastic Materials*"* (Cambridge University Press, New York, 2009).

[111] L.M. Hopkins, J.T. Kelly, A.S. Wexler, and A.K. Prasad, "Particle image velocimetry measurements in complex geometries," Exp. Fluids **29**(1), 91–95 (2000).

[112] C.C. Dierickx, M.C. Grossman, W.A. Farinelli, and R.R. Anderson, "Permanent hair removal by normal-mode ruby laser.," Arch. Dermatol. **134**(7), 837–842 (1998).

[113] Y. Tang, S. Lee, M.D. Nelson, S. Richard, and R. a Moats, "Adipose segmentation in small animals at 7T: a preliminary study.," BMC Genomics **11**(3), S9 (2010).

[114] W.D. Rooney, G. Johnson, X. Li, E.R. Cohen, S.G. Kim, K. Ugurbil, and C.S. Springer, "Magnetic field and tissue dependencies of human brain longitudinal 1H2O relaxation in vivo," Magn. Reson. Med. **57**(2), 308–318 (2007).

[115] M.A. Korteweg, J.J.M. Zwanenburg, P.J. Van Diest, M.A.A.J. Van Den Bosch, P.R. Luijten, R. Van Hillegersberg, W.P.T.M. Mali, and W.B. Veldhuis, "Characterization of ex vivo healthy human axillary lymph nodes with high resolution 7 Tesla MRI," Eur. Radiol. **21**(2), 310–317 (2011).